Article

Activity of Okgye Limestone Mine in South Korea Observed by InSAR Coherence and PSInSAR Techniques

Hoseung Lee, Jihyun Moon and Hoonyol Lee *

Department of Geophysics, Kangwon National University, Chuncheon 24341, Republic of Korea
* Correspondence: hoonyol@kangwon.ac.kr; Tel.: +82-33-250-8587

Abstract: The Okgye limestone mine, which is the largest open-pit limestone mine located in a mountainous area in Korea, suffered a collapse in 2012 that claimed four casualties. Restoration work on the rocky mined-out slopes, as well as mining and dumping activities, are still in progress. Monitoring slope stability is important to prevent the sudden collapse of slopes, which can be efficiently performed by satellite-based interferometric synthetic aperture radar (InSAR) techniques. Firstly, we obtained elevation changes using InSAR-generated Copernicus 30m DEM in 2014 and an SRTM 1Sec DEM in 2000, through which the area was roughly classified into the mining area, tailings storage area, and the mined-out area. A time series of 12-day coherence images produced by Sentinel-1B SAR were averaged annually to produce an RGB-composite image to observe the change in mining activities during 2018, 2019, and 2020. We found many persistent scatterers (PS) when observing the ground displacement, both in the ascending and descending orbits, from which we decomposed this into the vertical and east components. The largest displacement of 63.6 mm/year was observed during 2019 and 2020 in the tailings storage area in the direction of the dumping slope. For the rocky outcrops and the transmission tower, we found a seasonal oscillation, which can be interpreted as the thermal expansion of limestone and iron. This paper demonstrated that the surface stability and deformation of open-pit mines could be effectively monitored by combining InSAR DEM, coherence, and PSInSAR techniques.

Keywords: PSInSAR; InSAR coherence; elevation change; open-pit mine; activity; Sentinel-1

1. Introduction

Surface deformation due to slope instability and subsidence are the most important problems in the mining business [1]. Especially in the case of open-pit mines, high and steep slopes are very common, resulting in slope collapse and ground subsidence. Slopes are generated by ore mining benches and tailings storage areas. In the case of limestone mines, which form the target of this study area, the tailings are first dumped from the top of the storage and then redistributed and hardened by using a dozer. The hardening of the tailings is highly advantageous in terms of slope stability but is time-consuming and expensive [2]. The dumped tailings are composed of very loose materials that make for highly unstable slopes. Countermeasures are needed in areas where there is a high risk of landslides [3,4]. An appropriate method to reduce the damage from a landslide is to reduce the number of people exposed by implementing a landslide early warning system (EWS) based on stability monitoring [5]. The United Nations evaluates four key elements as essential for effective EWSs: risk assessment, on-site monitoring and forecasting, alert communication and alerting, and local response [6]. This study focuses on the monitoring of such hazardous areas by satellite-based synthetic aperture radar (SAR) images.

As a SAR system uses microwaves, it can penetrate clouds and obtain images day and night using active sensors [7]. Unlike the total stations frequently used in surveying open-pit mines, InSAR does not require physical reflectors to evaluate the phase of

backscattered signals due to the surface change [8]. InSAR has recently emerged as one of the most effective ways to monitor surface displacement [9,10]. Differential interferometric SAR (DInSAR) that removes the phase of elevation from the initial interferogram can be used to observe the line-of-sight (LOS) directional displacement within a precision of millimeters [11]. As a time-series InSAR technique, persistent scatterer InSAR (PSInSAR) observes displacements for stationary scatterers, such as artificial structures and outcrops, with at least 20 SAR images for statistical assessment [12]. Open-pit mines have good conditions for applying the PSInSAR technique because there are many persistent scatterers as the bedrock is exposed by removing vegetation for mining activities. Apart from the interferogram that utilizes the phase of a complex correlation coefficient using two SAR images of the same region, the amplitude of the complex correlation coefficient is defined as coherence [13]. InSAR coherence is widely used to evaluate the quality of interferograms and also provides information on the stability of the surface against the temporal changes of the backscattering targets. When using coherence, the activity of the study area over time can be observed as a random surface change that disturbs the integrity of the phase information [14].

Recently, many studies have been conducted to apply various SAR techniques in open-pit mines. Moon and Lee [15] observed the activity of open-pit mines by converting the coherence image into a normalized difference activity index (NDAI). The study focused on the surface disturbance due to mining activities but did not measure the displacement itself. Carla et al. [3,8] observed the displacement trend before the collapse of the open-pit mine slope by using satellite and ground-based InSAR. Paradella et al. [16] and Hartwig et al. [17] observed the displacement of the tailings storage area, where subsidence occurred by using InSAR and PSInSAR techniques. These papers analyzed the tailings storage area with InSAR phase data to assess collapse risk only within relatively stable areas where persistent scatterers can be found.

This study observes the overall activities of an open-pit limestone mine in Okgye, Gangneung-si, Republic of Korea, by combining various InSAR techniques, such as InSAR DEM, InSAR coherence, and PSInSAR, to access the mining activities for both stable and unstable surfaces. The mining and tailings storage areas are roughly distinguished by elevation changes between two global DEMs obtained in 2000 and 2014, respectively. A series of Sentinel-1 coherence images with a 12-day temporal baseline were processed to analyze the activity between 2018 to 2020. PSInSAR was then applied to produce two-dimensional surface displacement maps of the open-pit mine using both ascending and descending data from Sentinel-1. Section 2 explains the study area and the data used for this study. Section 3 describes the method of elevation change, coherence imagery, and the PSInSAR techniques. Section 4 presents the results of the findings from the mining, tailings storage, and restoration activities in terms of volumetric change, surface displacement, and thermal expansion signals. Section 5 discusses the major issues and concerns of the study, while Section 6 concludes this study.

2. Materials

2.1. Study Area

Okgye mine is an open-pit mine for excavating limestone resources for cement production. Located on Mt. Seokbyeong in Okgye, Gangneung-si (Figure 1), it is the largest open-pit mine in the Republic of Korea. Annually, it produces 6.6 million tons of cement clinker, which is an intermediary product for Portland cement [18]. The geology of the study area consists of the Wonpyong Formation of the Paleozoic Ordovician, the Pungchon Formation of the Cambrian, and the Myobong Formation. Among them, the Pungchon Formation is the main strata for limestone mining, with an average thickness of 600 m. It can be divided into an upper limestone zone (Cph), a middle dolomite zone (Cpd), and a lower limestone zone (Cpl), depending on the rock phase. The high-grade limestone

of Cph is used for the chemical industry, while Cpl is a major mining layer for producing cement [19].
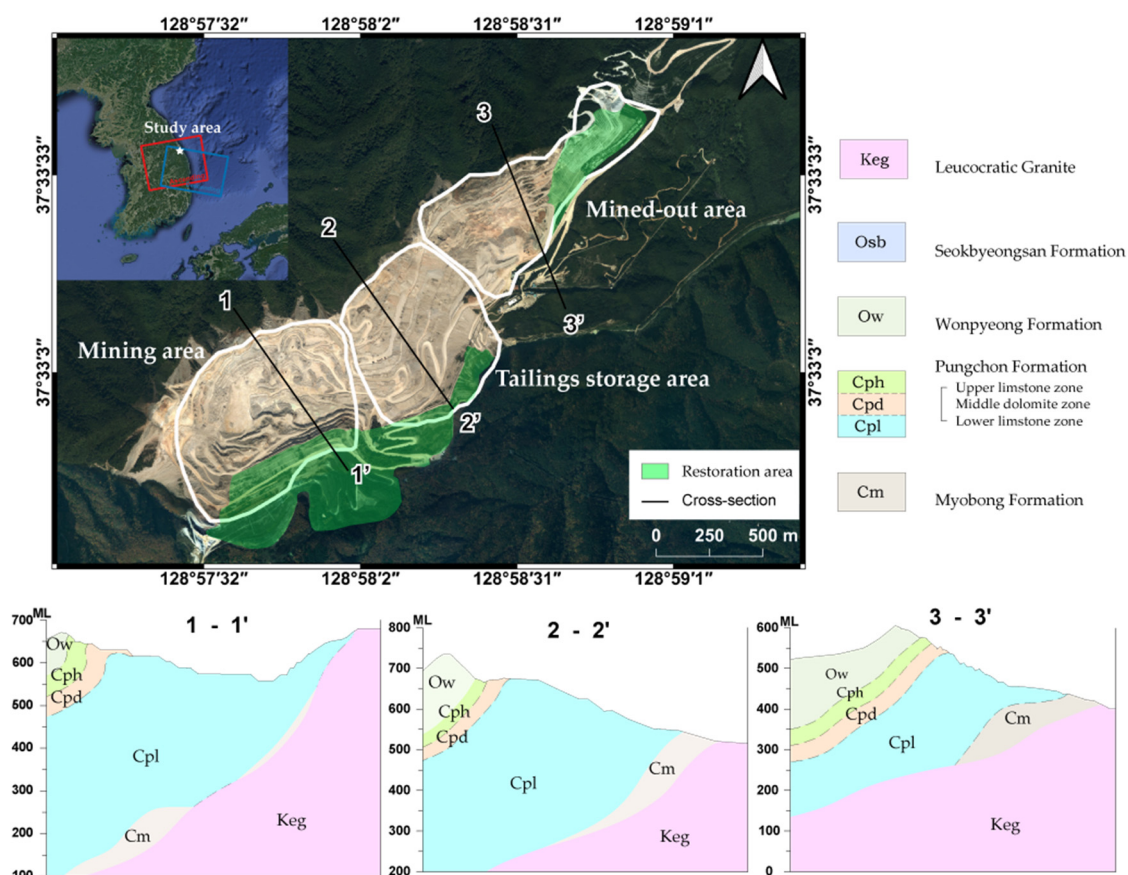
Figure 1. The study area is divided into the mining area, tailings storage area, and mined-out area. Geological profiles were drawn along the three lines. The red box represents the ascending pass of the Sentinel-1 SAR images, while the blue box is the descending pass. The background image is a satellite image from 2019 using Google Earth.

Okgye open-pit mine has an area of about 230 ha, in a long elliptical shape with a major axis of 3 km in a northeast direction and a minor axis of 1 km in a northwest direction. More than 85% of the area is above 400 m (sea level) [20]. The mine can be largely divided into three areas: the mining area in the west, where active mining is in progress, the tailings storage area in the middle, where dumping activities occur, and the mined-out area in the east, where restoration work is in progress.

Mining activities were performed by excavating materials after blasting a series of benches. The maximum height before the mining activity was 830 m above sea level, which was lowered by more than 200 m, especially in the mining area in the west. On August 23, 2012, a collapse on the southern slope of the mining area caused the loss of four casualties. This area has been actively excavated since 2003, making a slope angle of 38°~45°. This area was restored in 2014 by planting trees on the mitigated slopes after the accident. The top of the tailings storage area is currently dumping continuously, with a slope angle of about 25°. The southern part of the tailings storage area was restored in 2005. Currently, the mined-out area in the east is undergoing a vegetation restoration project. Generally, it uses the tailings generated during the mining process to mitigate the slope to 1:3. On top of the tailings, the soil was covered with a thickness of 80 cm. Topsoil and loam were then mixed in a 1:1 ratio and covered with a thickness of 10 cm to form a vegetation base. Finally, large stones were laid every 7 m (in height) for the stability of the slope [21,22], which might have caused slow deformation due to gravity.

2.2. Dataset

Two open-access InSAR-generated digital elevation models (DEMs) were used to calculate the change in elevation of the Okgye mine and roughly estimate the mining and dumping activities. The shuttle radar topography mission (SRTM) DEM was acquired from two C-band antennas and represents the altitude collected from 11–23 February 2000 [11]. SRTM DEM is currently available in several versions on Earth Explorer [23], United States Geological Survey (USGS). Among them, the SRTM 1 Sec HGT DEM with a spatial resolution of 30 m was used in this study. The nominal absolute vertical accuracy of it is 9 m [11]. The Copernicus DEM of the study area is based on GLO-30, which represents the average of data from 29 August 2011 and 22 August 2014 obtained by the bistatic mission of TanDEM-X and TerraSAR-X. Among the various versions available in CREODIAS [24], a Copernicus 30 m DEM was used, for which the absolute vertical resolution is 2 m. Both DEM data can also be automatically downloaded from the European Space Agency (ESA) SNAP (SeNtinel Application Platform) software. Other local DEMs were also obtained from the National Geographic Information Service of Korea [25], which has 1 m resolution for the years 2006, 2010, 2012, 2014, 2016, and 2019.

A series of Sentinel-1 SAR images provided by the European Space Agency (ESA) were used to observe the activity and surface displacement of the Okgye mine (Table 1). All SAR images used in this study are single-look complex (SLC) data obtained in interferometric wide-swath (IW) mode with VV polarization in the C-band. In the descending track, a total of 91 images were obtained by Sentinel-1B during the period between 3 January 2018 to 30 December 2020, all with a 12-day temporal baseline. For the ascending track, we obtained 41 images from 4 January 2019 to 24 December 2020. Most of the images on the ascending track were taken by Sentinel-1A, except for one on 7 September 2019, taken with Sentinel-1B. Not all of the ascending data have a 12-day temporal baseline. Therefore, we only used descending data for coherence imagery due to the missing data from the ascending Sentinel-1A, with a temporal baseline larger than 12 days, and due to the geometric problem in interpreting both the ascending and descending coherence images. For PSInSAR, we used both ascending and descending data only for two years, from 2019 to 2020, to obtain as many PS as possible to produce two-dimensional displacements of the stable targets. Currently, Sentinel-1 SAR data are provided free of charge from the Copernicus Open Access Hub [26] of the ESA or the Alaska Satellite Facility (ASF) [27].

Table 1. Sentinel-1 SAR dataset used in this study.

Technique	Satellite	Pass	Orbit	Frame	Date (YYYY/MM/DD~YYYY/MM/DD)	Number of Data
Coherence	Sentinel-1B	Descending	61	470	2018/01/03~2020/12/30	91
PSInSAR	Sentinel-1B	Descending	61	470	2019/01/10~2020/12/30	66
	Sentinel-1A/B	Ascending	54	117	2019/01/04~2020/12/24	41

3. Methods

3.1. Elevation and Volume Change

Active open-pit mines show elevation changes due to continuous mining and accumulation. Subtracting two different DEMs can detect surface elevation changes during the acquisition period [15,28,29]. The elevation change was obtained as the difference between the SRTM 1 Sec HGT DEM and the Copernicus 30 m DEM. Data processing was performed by using the band math function of the SNAP software [15].

The calculation of volume change was conducted on QGIS software, an open-source desktop geographic information system application. First, the coordinates were reprojected to the Korean 2000/Unified CS coordinate system to change the unit of the map to a scale in meters. The area of interest with a large elevation change is designated as a polygon to calculate the area. The area with vegetation was excluded from the calculation

because it contains errors from the seasonal effects of vegetation cover and/or the difference in penetration depth into the vegetation canopy between the C-band of the SRTM DEM and the X-band of the Copernicus DEM. Finally, volume change was calculated by integrating the elevation changes of each pixel in the polygon. Volume changes can be converted into metric tons by assuming the density and porosity of the rocks and tailings.

3.2. Coherence and RGB Compositing

Coherence indicates the phase correlation between two SAR images of the same area taken at different times. Coherence has a value ranging from 0 to 1, where a stable building or road has a high value (close to 1), and randomly varying leaves in vegetation and disturbances of surface soil have a low value (close to 0) [7,15]. A total of 91 SLC Sentinel-1B data obtained in a descending orbit from 3 January 2018 to 30 December 2020 were coregistered using the S-1 back-geocoding tool of SNAP. Coherence and DInSAR images, all with a 12-day temporal baseline, were obtained by subtracting the flat-earth phase from the interferogram formation and subtracting the topographic phase using Copernicus 30 m DEM. Black-fill demarcation between the generated images was removed by the deburst function, and the noise was removed through Goldstein phase filtering using the SNAP software.

To reduce the noise of the coherence image and to see the average activity area for a specific period, coherence images were averaged over a year (Figure 2). In the annually averaged coherence image, black indicates the active area, showing random surface change, while white is the stable area. In order to visually display the activity and analyze the time series, a composite image was produced by setting the RGB color to the averaged coherence images of each year: blue for 2018, green for 2019, and red for 2020. By analyzing the various colors observed in the RGB composite image of the annually averaged coherence images, the activity of each region could be identified efficiently.
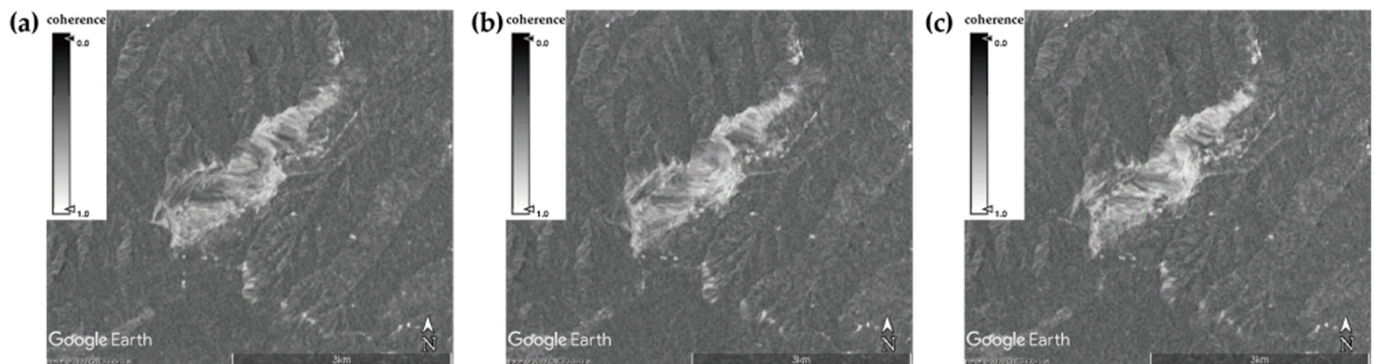
Figure 2. Annually averaged 12-day coherence images of the study area in (**a**) 2018, (**b**) 2019, and (**c**) 2020.

3.3. PSInSAR Using Both Ascending and Descending Orbits

PSInSAR is a technique that can estimate the time-series displacement of the surface by stacking $N+1$ SLC images into a common master image to produce N interferograms. In this study, the PSInSAR technique was performed using StaMPS (Stanford Method Persistent Scatterers) [30]. StaMPS is a software package that implements the PSInSAR technique and was developed at Stanford University. It is currently being distributed for free on Github, and many studies using it have been carried out [31–34].

Orbital information and external DEM can be used to remove the influence of the Earth's curvature from the produced interferogram. The phase of the SAR interferogram is affected by several factors, such as linear phase ramp (LPR), external DEM inaccuracy, atmospheric phase screen (APS), displacement by surface deformation, and speckle and decorrelation noise [12,30].

To apply the PSInSAR technique, preprocessing is required in SNAP software before the data are put to StaMPS. An optimal single master image is designated in consideration of the perpendicular baseline and temporal baseline. DInSAR was then performed by stacking the total slave image onto the master image (Figure 3). The output data, such as intensity, DInSAR, DEM, LON, and LAT, were converted into a form that can be processed by StaMPS. In StaMPS, persistent scatterer (PS) pixels are selected based on the amplitude dispersion index (ADI), calculated from the standard deviation and average of the amplitude [12,30]. The lower the ADI is, the more stable the pixel is without activity. The pixels with an ADI of less than 0.4 were selected as PS in this study. For the DInSAR data of each PS point selected, phase unwrapping was performed with SNAPHU (Statistical-cost Network-flow Algorithm for Phase Unwrapping) to obtain LOS velocity maps for PS. After that, a DEM error map and a phase ramp map were prepared and removed from the LOS velocity map. Studies are underway to mitigate the effects of the atmosphere by various methods such as MODIS, TRAIN, and GACOS [35-37]. To remove the atmospheric effect, the power-law model of TRAIN and the iterative tropospheric decomposition (ITD) model of GACOS [38] were used. However, no significant improvement was made because the study area is too small when compared with the 10 km resolution of the models at best. The parameters used for StaMPS processing are detailed in Table 2 [39].

Table 2. Parameters Used in the StaMPS Processing.

Parameter	Scla_Deramp	Unwrap_Gold_n_Win	Unwrap_Grid_Size	Unwrap_Time_Win	Scn_Time_Win
Default	'N'	32	200	730	365
Used	'Y'	8	10	24	50

Since InSAR can only measure a projection of displacement along the LOS direction, at least three measurements at different LOS directions are necessary to estimate a true displacement vector. LOS displacements of the ascending and descending data were analyzed by decomposing them into horizontal and vertical components [40–42].

Given a Cartesian coordinate system (x, y, z), pointing east, north, and zenith, respectively, and centered at a surface target system, the LOS vector from surface to satellite is defined as

$$\hat{l} = (-\sin\theta\cos\alpha, \sin\theta\sin\alpha, \cos\theta), \tag{1}$$

where θ is the incidence angle measured from the z-axis to the LOS direction, and α is the satellite heading projected on the horizontal plane measured clockwise from the north. Then, the interferometric phase of the ascending and descending orbit, ϕ_a and ϕ_d, are

$$\phi_a = \frac{4\pi}{\lambda}\hat{l}_a \cdot \vec{s},$$

$$\phi_d = \frac{4\pi}{\lambda}\hat{l}_d \cdot \vec{s}. \tag{2}$$

Here, $\vec{s} = (s_x, s_y, s_z)$ is the surface displacement vector. Equation (2) can be rewritten in matrix format:

$$\begin{pmatrix} \phi_a \\ \phi_d \end{pmatrix} = \frac{4\pi}{\lambda} \begin{pmatrix} -\sin\theta_a\cos\alpha_a & \sin\theta_a\sin\alpha_a & \cos\theta_a \\ -\sin\theta_d\cos\alpha_d & \sin\theta_d\sin\alpha_d & \cos\theta_d \end{pmatrix} \begin{pmatrix} s_x \\ s_y \\ s_z \end{pmatrix} \tag{3}$$

This equation is ill-posed and cannot be solved for surface displacement. An approximation emerges from the fact that the Sentinel-1 satellite is polar orbiting with an inclination of 98.18°, such that α is 350.11° for the ascending orbit and 189.49° for the descending orbit. Therefore, $\sin\alpha \approx 0$ in Equation (3), and the contribution of s_y for the phase in Equation (3) is very low when compared to the other components. Equation (3) [40] can be approximated as the following:

$$\begin{pmatrix} \phi_a \\ \phi_d \end{pmatrix} \approx \frac{4\pi}{\lambda} \begin{pmatrix} -\sin\theta_a \cos\alpha_a & \cos\theta_a \\ -\sin\theta_d \cos\alpha_d & \cos\theta_d \end{pmatrix} \begin{pmatrix} s_x \\ s_z \end{pmatrix} \tag{4}$$

The surface displacement components of the east and vertical directions can be estimated by inverting the above matrix equation.

$$\begin{pmatrix} s_x \\ s_z \end{pmatrix} \approx \frac{\lambda}{4\pi} \begin{pmatrix} -\sin\theta_a \cos\alpha_a & \cos\theta_a \\ -\sin\theta_d \cos\alpha_d & \cos\theta_d \end{pmatrix}^{-1} \begin{pmatrix} \phi_a \\ \phi_d \end{pmatrix} \tag{5}$$

Maps of surface deformation rate measured by PSInSAR in mm/year for the ascending and descending LOS directions will be converted to east–west and up–down components by using Equation (5). It would be rare to have PSs that exactly match the location both in the ascending and descending orbit simultaneously. Therefore, interpolation is performed by using inverse distance weighting (IDW) on the maps. Only populated PS regions are used for interpretation.
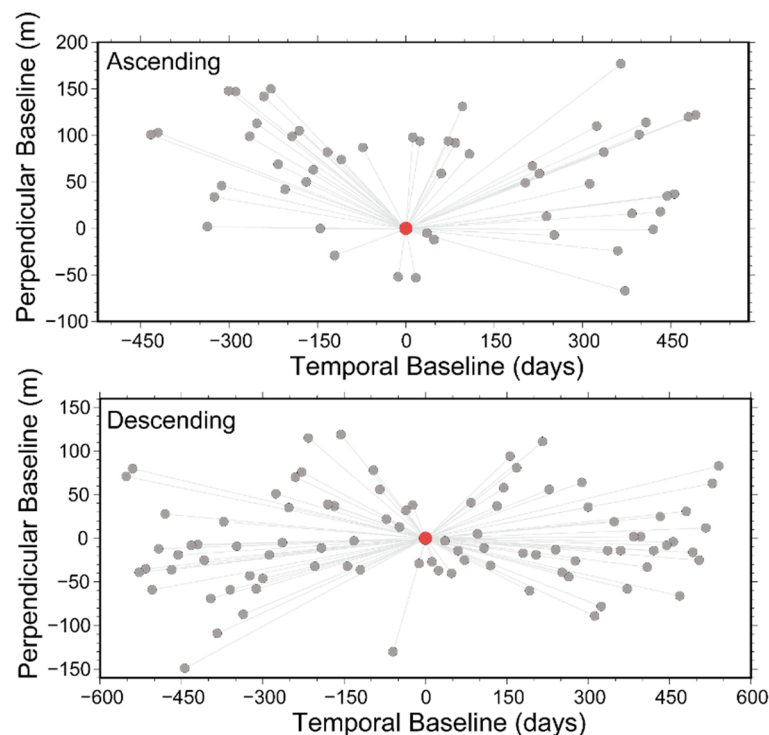

Figure 3. Distribution of the temporal and perpendicular baselines of Sentinel-1 SAR data used for PSInSAR. The red dots indicate the master data from 19 October 2019 for the ascending orbit and from 5 January 2020 for the descending orbit.

4. Results

Figure 4 shows the results of the InSAR DEM change, the RGB composite of the annually averaged 12-day coherence images, the PSInSAR results from ascending and descending orbits, and the corresponding east and vertical components of the displacement rates. Figure 4a shows the elevation change between 2000 and 2014 calculated by the two InSAR DEMs. The mining area in the west and the mined-out area in the east show a decrease in elevation due to mining activity, while the tailings storage area is distinguished by a surface elevation rise. Figure 4b shows the RGB composite of the annually averaged coherence images with red for 2020, green for 2019, and blue for 2018. White represents the stable areas with no activity, such as the mined-out area where bare rocks are exposed and the areas after the restoration work have been carried out. Different colors indicate various histories of excavation and dumping activities during 2018 and 2020, especially in the northeast of the mining area and the tailings storage area. Black represents the always active area due to continuous mining and dumping activities.

Figure 4c,d shows the PSs observed in the stable area between 2018 and 2020. Obviously, the PSs are populated in the white region of the RGB composite of the coherence image in Figure 4b, such as the bare rocks and restored slopes. PSInSAR shows relatively stable bare rocks and possible landslides in the tailings storage area due to its loose material. The PSInSAR results from the ascending and descending orbits were combined to produce the horizontal east and vertical components, as shown in Figure 4e,f. The subsidence and east components are dominant in the tailings storage area, which implies landslides along the slope of the dumping sites. A detailed description of the findings will be discussed in the following sections.
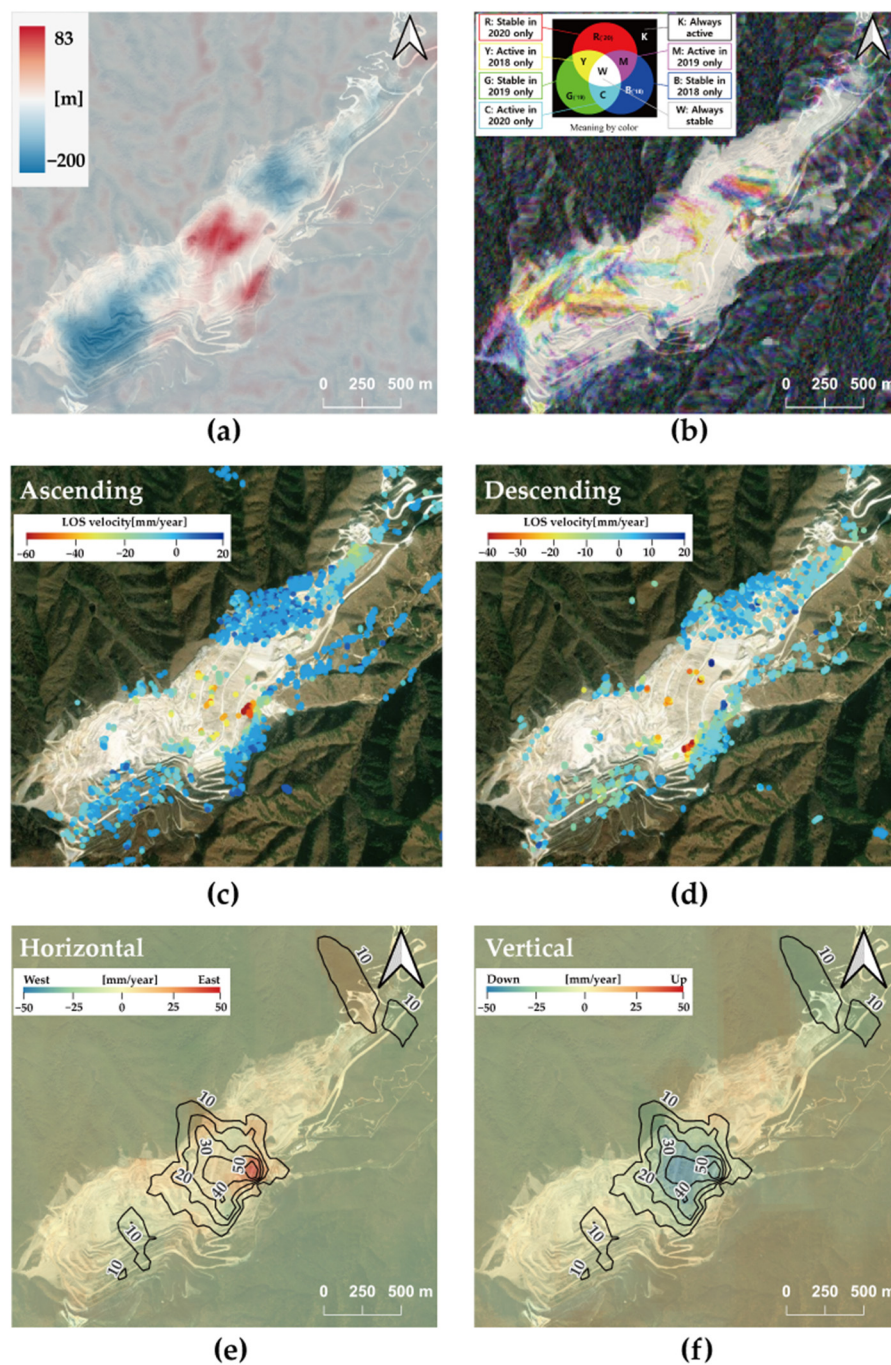
Figure 4. The overall result images from the study area. (**a**) Elevation change from the InSAR DEMs, (**b**) RGB composite of the annually averaged coherence images with R for 2020, G for 2019, and B

for 2018, (**c**,**d**) PSInSAR result images, and (**e**,**f**) the interpolated horizontal (east) and vertical components of PS.

4.1. Elevation and Volume Change during 2010 to 2014

Okgye mine is roughly divided into three regions for the calculation of elevation and volume changes: the mining area, the tailings storage area, and the mined-out area (Figure 5). Several cross-sections are drawn to observe the profiles of the distinct elevation changes in this section and later on. A-A' shows the overall elevation change of the open-pit mine. In the southwest of the mining area, a decrease in elevation of up to 200 m occurred from 2000 to 2014. The elevation has been lowered even further due to the active mining of this region up until recently. The tailings storage area had an elevation rise of about 83 m in the north and an elevation rise of about 72 m in the south. In the mined-out area, an elevation decrease of about 126 m in the south and about 46 m in the north occurred.

The volume changes were calculated to be −19,959,439 m^3 in the mining area, 17,102,892 m^3 in the tailings storage area, and −6,240,931 m^3 in the mined-out area, as shown in Table 3. When summing all these values, there is a simple volume deficit of −9,097,478 m^3 from 2000 to 2014. However, this deficit is meaningless and should be adjusted in terms of the porosity difference between hard rock and dumped loose materials. Given the volume of the original hard rock, *R*, and the cavity volume, *c*, added due to mining, the porosity of the dumped loose materials is

$$n = \frac{c}{R + c} \tag{6}$$

Roughly applying 30% porosity (*n* = 0.3) for the tailings storage area, the volume of the dumped material in the tailings storage area being hard rock (*R*) would have been reduced to 11,972,024 m^3, as shown in Table 3. The volume deficit in the form of hard rock would be −14,228,346 m^3 for 14 years, which can be possibly assumed to be the material used for the production of cement. In terms of mass, by multiplying the volume changes with an average value of 2.75 ton/m^3 for the density of limestone, a total mass deficit of −39.13 million tons might have been used for the production of clinker during the period from 2000 to 2014. Annually, it would be −2.61 million tons per year. Considering the 6.6 million tons of annual clinker production mentioned in Section 2.1, this might indicate the clay-to-limestone ratio of the clinker (defined as clay/(clay + limestone)) to be roughly 0.60. However, the above calculation is too rough with so many assumptions for density and porosity, which need to be verified and adjusted thoroughly for practical use.
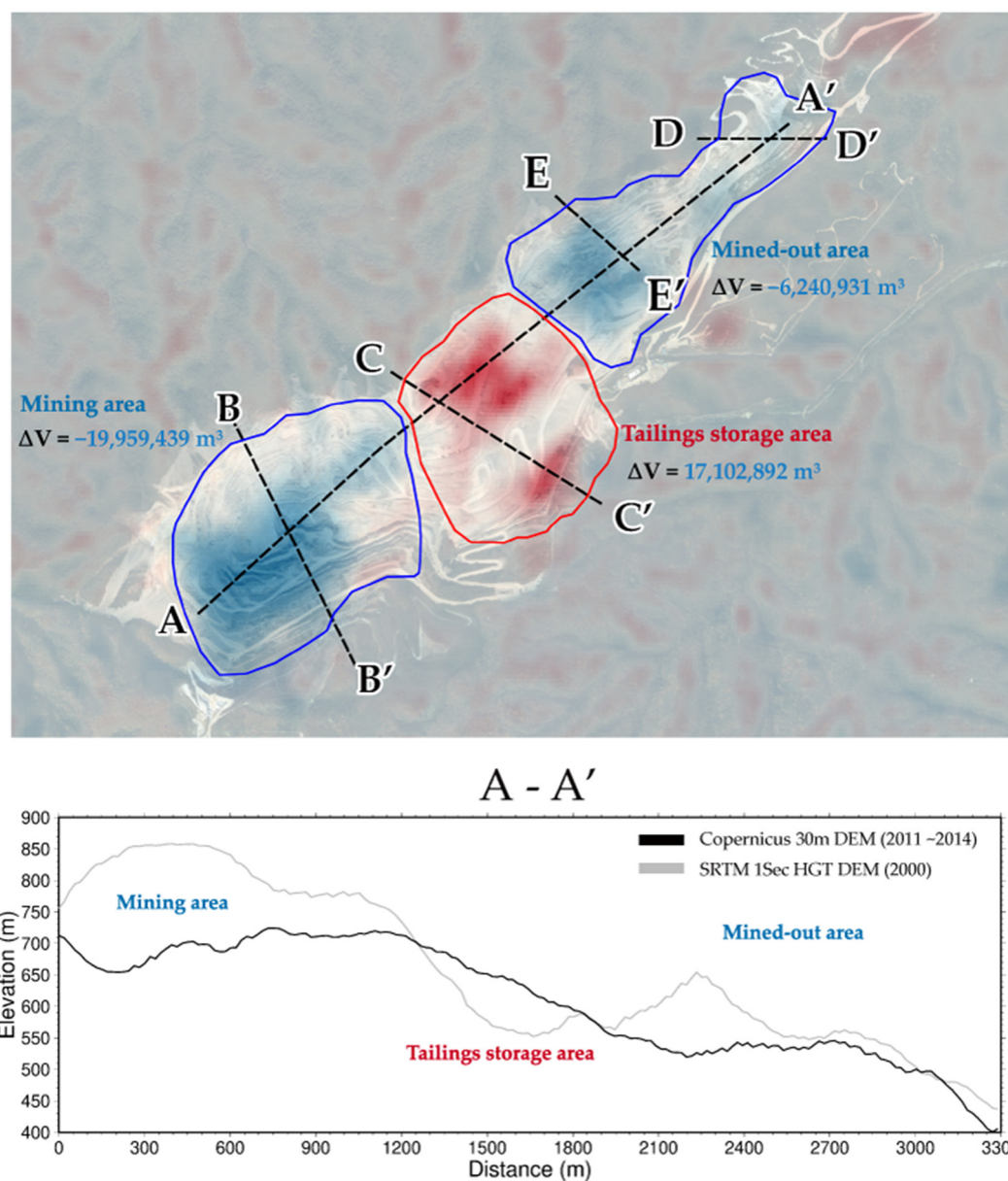
Figure 5. Elevation change map between 2000 and 2014 with separate polygons for the volume change calculation. The profiles of the elevation are drawn along the dashed lines in the below and following figures.

Table 3. Volume and mass changes between 2000 and 2014.

Type	Mining Area	Tailings Storage Area	Mined-Out Area	Total
Hard Rock (R) [m³]	−19,959,439	11,972,024 *	−6,240,931	−14,228,346
Cavity (c) [m³]	−8,554,045 *	5,130,868 *	−2,674,685 *	−6,097,862
Dumped Material ($R+c$) [m³]	−28,513,484 *	17,102,892	−8,915,616 *	−20,326,208
Mass [million ton]	−54.89 **	32.92 **	−17.16**	−39.13

* values calculated assuming the porosity $n = 0.3$ from the InSAR DEM measurements in blue color.
** values calculated by multiplying the density of limestone 2.75 ton/m³ to the hard rock volumes.

4.2. The Mining Area

The mining area in the west of Okgye mine was the most active excavation area during the study period (Figure 6). Excavation is in progress in the northern and central parts of the mining area, while the southern part represents the slope restored in 2015 after the

mining. Between 2000 and 2014, the largest elevation loss was observed in the southwest area from the center, as shown in Figure 6a. Between 2018 and 2020, mining occurred mainly in the northern part and the center, as shown in Figure 6b, using various colors. Magenta (active in 2019 only) and yellow (active in 2018 only) are distributed in the center and west, while cyan (active in 2020 only), magenta, and blue (active in 2019 and 2020) are distributed toward the northeast direction. It can be assumed that mining activity moved from the center and west in 2018 toward the northeast direction in 2020, as shown in Figure 6b,d.

In the right corner of the mining area, there is a station where trucks transport the excavated materials onto a conveyor belt system that transports limestone to the concentrator plant, as indicated in Figure 6b. The black polygons are the roads to the station, which show various color patterns. Magenta, yellow, and cyan are distributed along the roads to the station, indicating that the roads were built to support the mining activity separately at those times. The mining area is still actively excavating, as seen in the optical photos taken in 2019, 2021, and 2022 in Figure 6c–e. In the restored area located in the southwest part of the mining area, the blue and magenta colors are observed due to the growth in vegetation after 2019. Vegetation growth over some parts of the restored area can be confirmed in a field photo of the mining area taken in 2022, as shown in Figure 6e.

Figure 6c shows the distribution of the PSs, both from the ascending (triangle) and descending (circle) orbits. The PSs are distributed only in stable (white) areas in the coherence map and not in the active (colored) areas. The PSs were mainly observed on the restored slopes facing northwest, as shown in the right side of the field photo in Figure 6e. Each LOS displacement was used to obtain the east and vertical components, which is depicted on a cross-section B-B' in Figure 7, where the PSs are densely populated. Displacement of 5~11 mm/year occurred in the west direction along the restored slope. This is the smallest value when compared with the other restoration slopes, which will be shown later, probably because the subsidence direction is expected to have a strong north-south component which is not detectable by the current SAR orbits. Another possibility is that the restoration was performed directly over a hard rock bench without dumping the tailings, which is different from the other restoration areas in the mined-out area, as will be shown in the next section.
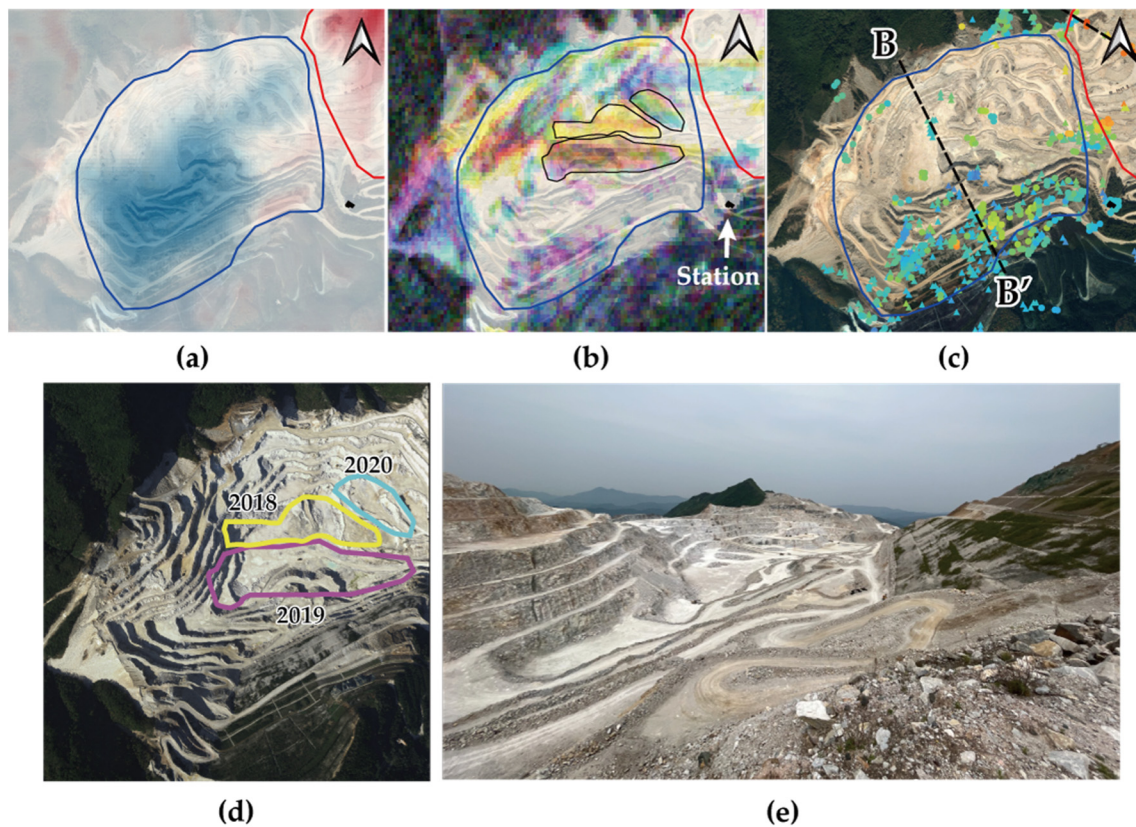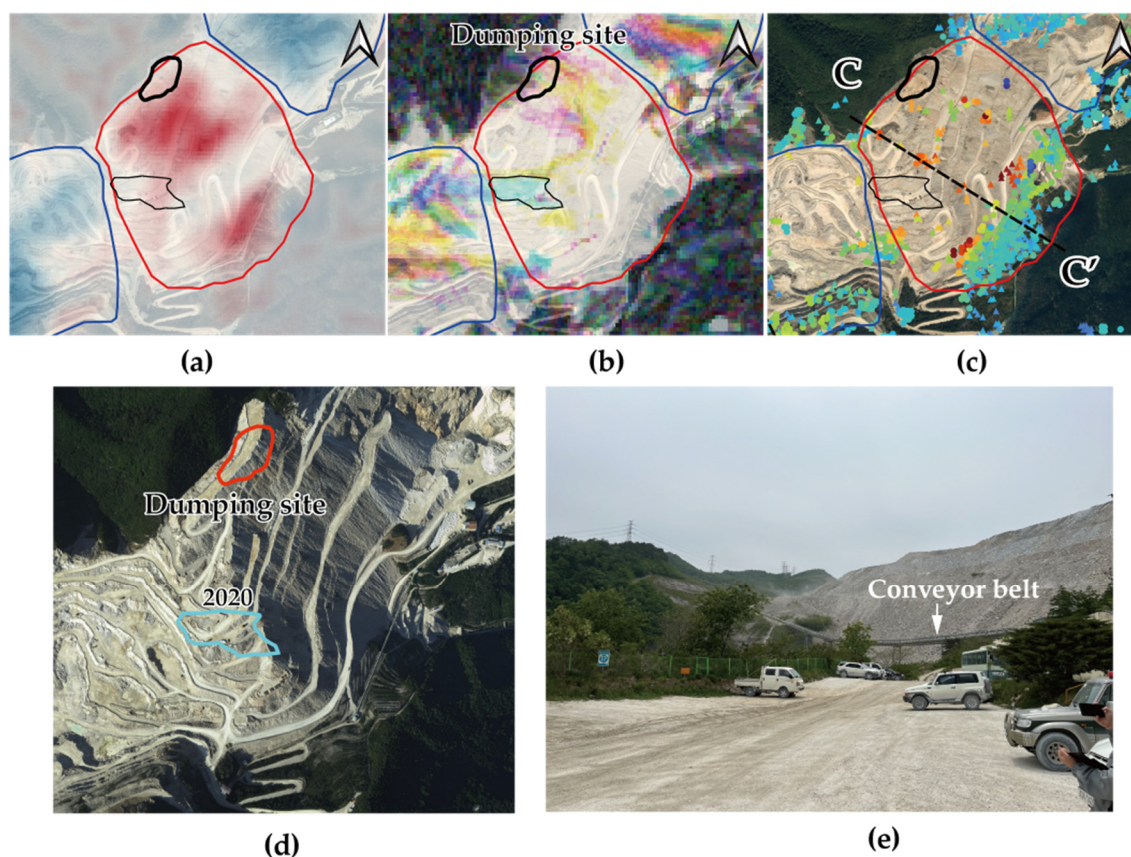
Figure 6. The resulting images of the mining area. (**a**) Elevation change, (**b**) RGB composited coherence image, (**c**) PSInSAR points from ascending (triangle) and descending (circle) orbit overlying a Google Earth satellite image from 2019, (**d**) an aerial photograph of 2021, and (**e**) a field photo taken in 2022.
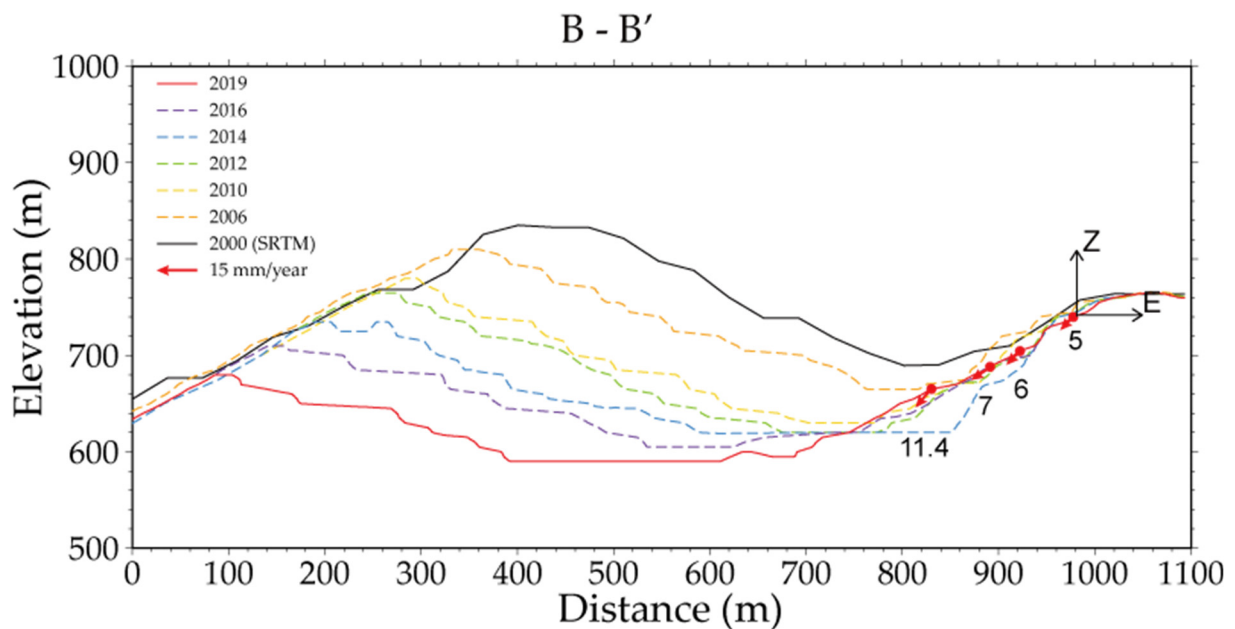
Figure 7. Elevation changes and displacements along the B-B' cross-section in the mining area. Note the displacement arrows are in vertical-east plane. Except for SRTM, the rest of the DEM was obtained from the National Geographic Information Service of Korea.

4.3. The Tailings Storage Area

The tailings storage area in the middle of the mine is divided into two parts: the dumping site in the north and the restored area in the south. The restoration of the southern slope was carried out in 2012 after the completion of the dumping of the tailings (Figure 8). Figure 8a shows that there was a large elevation increase in the northwest area and also in the south area between 2000 and 2014 due to dumping activities. Between 2018 and 2020, a decorrelation of InSAR occurred due to the activities in the north and the west area, as shown in Figure 8b. The RGB composite map of the annually averaged coherence shows progressive activity for dumping and road construction in 2018 (yellow), 2019 (magenta), and 2020 (cyan). Dumping activity progressed towards the northeast of the dumping site, which formed a bench by dumping and flattening the tailings. In the vicinity of the dumping site in Figure 8b, the yellow and magenta colors are distributed along the slope, which is thought to be the tailings that flowed down the slope in 2018 and 2019. The expansion of the dumping site can be seen as a red dotted line in the aerial photo of Figure 8d taken in 2021. The western area has a cyan-colored area representing the creation of a road from the mining area toward the dumping site and the station in 2020. The southern restoration slope shows a white color, indicating that there was no activity from 2012 after the completion of the restoration.


Figure 8. The resulting images of the tailings storage area. (**a**) Elevation change, (**b**) RGB composited coherence image, (**c**) PSInSAR points from ascending (triangle) and descending (circle) orbit overlying a Google Earth satellite image of 2019, (**d**) an aerial photograph of 2021 with polygons indicating recent dumping sites, and (**e**) a field photo taken in 2022.

Figure 8c shows that the PSs were mainly observed in the white color area of Figure 8b, which is a stable area. The PSs were observed on the southern slopes of the restored area, where restoration work was completed in 2012, and the northern slopes, where dumping activity finished before 2018. In particular, a lot of PSs were observed along the conveyor belt in the south, while only a few occurred on the northern slope (Figure 8e).

The PSs are distributed less on the northern slope and are densely distributed on the southern restoration slope.

Figure 9a shows the displacement of the tailings slopes along C-C' observed from 2019 to 2020. The northern slope on the left of the cross-section shows 18 mm/year displacement on the top of the slope and 36.2 mm/year at the bottom. The displacement vector has more horizontal components at the bottom than at the top of the slope. The displacement is maximum at C1, where the thickness of the deposited tailings is the largest area; the dumping activity was finished only recently in 2018. This implies that the amount of displacement along the slope is determined by the thickness of the deposited tailings. The southern restored slope, located at the right side of Figure 9a, was restored by filling tailings in 2012. The ground is relatively stable and shows a slight displacement of less than 7 mm/year in the west direction. An eastward displacement of 14.5 mm/year is observed at the center of the restored slope. This is thought to be the cumulative displacement affected from the western slope. Generally, the direction of displacement follows the slope of the original topography and the dumping slope, with a few exceptions due to errors from PSInSAR or IDW.
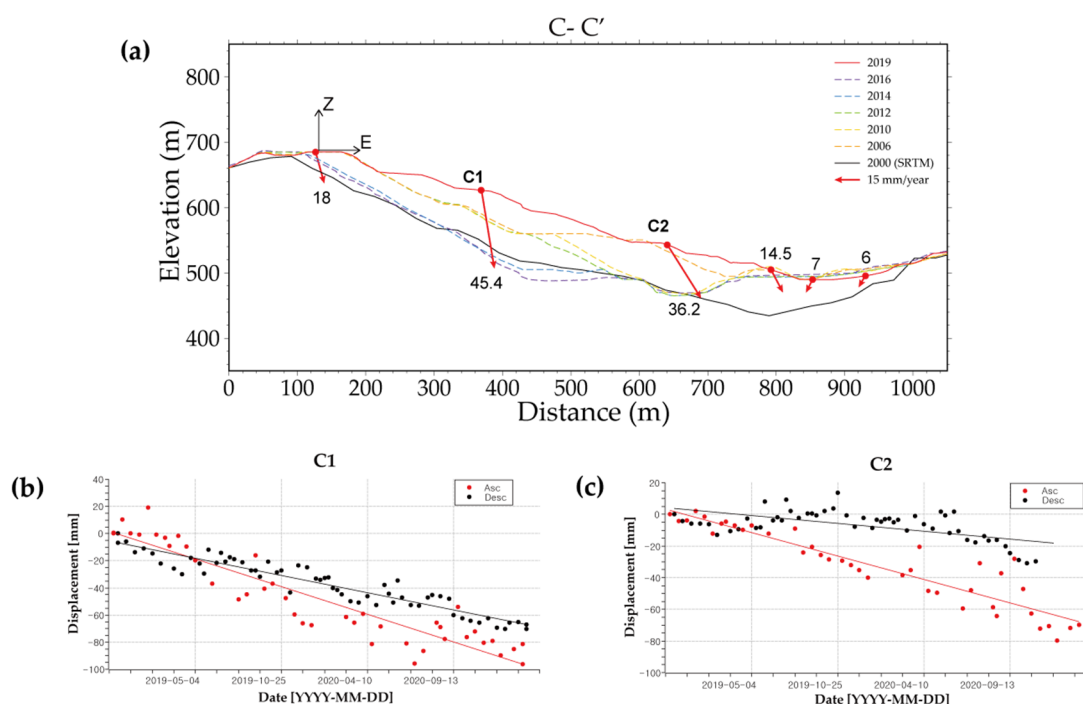

Figure 9. Elevation change and displacement along the C-C' on the slope of the tailings storage area. (**a**) Cross section of C-C', and change along the slope and time-series plots of displacement in (**b**) C1 and (**c**) C2 from the ascending and descending orbits with arbitrary offsets. The DEM was obtained from the National Geographic Information Service of Korea, except for the SRTM in 2000.
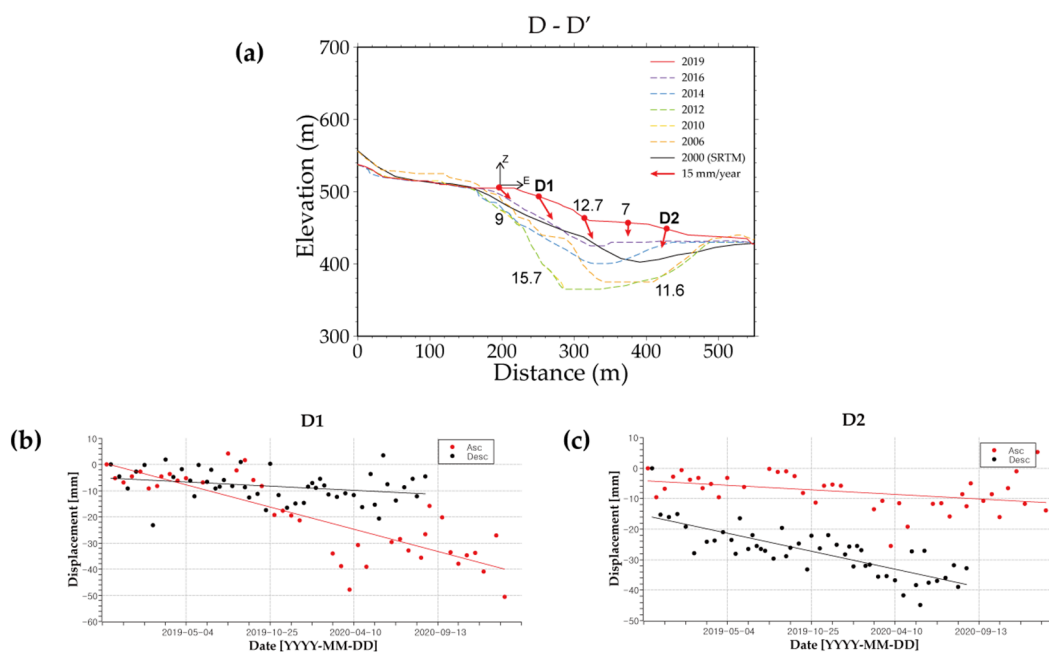
4.4. The Mined-Out Area

The mined-out area is where the excavation mining activities were completed well before 2010. From 2000 to 2015, the largest decrease in elevation occurred in the southwest, and a slight decrease occurred in the northeast, as shown in Figure 10a. The northeastern area started mining after 2000 and completed the filling of the tailings in the mined valley before 2015. The overall restoration work on the northeastern slope was completed in 2017. The southwestern area, formally a mining site, became a dumping site again after 2019, as shown in Figure 10b–e. Dumping activity from 2018 to 2020 was mainly observed in the southwestern area, as shown in Figure 10b. Magenta (active in 2019 only) and blue (active in 2019 and 2020) are distributed along the slope due to the tailings that flow along the slope in the process of dumping and flattening from 2019. The optical images from

2019 and 2021 in Figure 10c,d confirmed that the dumping site was expanded in a north-east direction, as shown by a red dotted line in Figure 10d.
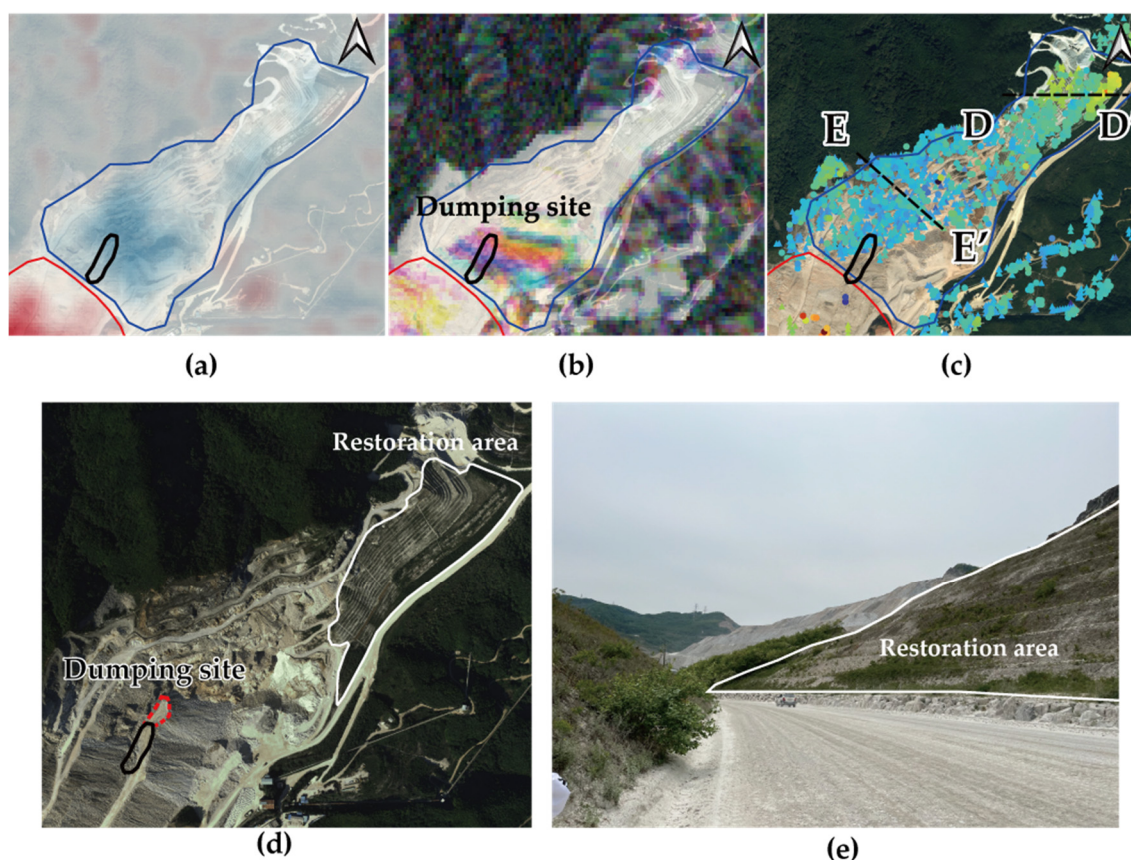
Figure 10. The resulting image of the mined-out area. (**a**) Elevation change, (**b**) RGB composite image and dumping site, (**c**) PSInSAR result image and cross-section, (**d**) 2021 aerial photograph and red dotted line are expanded dumping area, and (**e**) 2022 field photo.

PS was observed in all areas except the dumping sites, as shown in Figure 10c. The rocky mined-out area in the middle of the image has many PSs that do not show any displacement. However, subsidence occurred on the northeastern restoration. For slope restoration, the bedrock is covered with 90 cm thick soil. For the stability of the slope, tracing works are performed by putting blast stones in a row every 7 m (in height) [21,22]. These blast stones are thought to be observed as PS. Figure 11a shows the displacement of the PSs in a cross-section across the restoration area. The magnitude of the displacement increases and then decreases along the lateral line, and the direction changes from east to west. The reason for this lies in the development process of the past. The elevation change DEMs in Figure 11a shows that the region was deeply mined from 2000 to 2012, and subsequent dumping occurred in this valley from 2012 to 2019. The magnitude and direction of the displacement follow the depth and the bottom topography of the dumped tailings in this old valley.

Figure 11. Elevation change and displacement along the D-D' on the slope of the mined-out area. (**a**) Cross section of D-D', and change along the slope and time-series plots of displacement in (**b**) D1 and (**c**) D2 from the ascending and descending orbits with arbitrary offsets. The DEM was obtained from the National Geographic Information Service of Korea, except for the SRTM in 2000.

4.5. Thermal Expansion of Limestone and Iron

Figure 12 shows the time-series plots of LOS displacement from descending orbit for the PSs in the bare rocks in the mined-out area. They show the sinusoidal behavior of expansion in summer and subsidence in winter. This seasonal tendency is thought to be the thermal expansion of limestone. Such thermal expansion of ground targets has been reported in several PSInSAR studies using C-band and X-band [43–45]. We selected three PSs along the E-E' cross-section in the rocky area with different elevations and a stable PS at the lower part of the valley, as shown in Figure 12a,b.
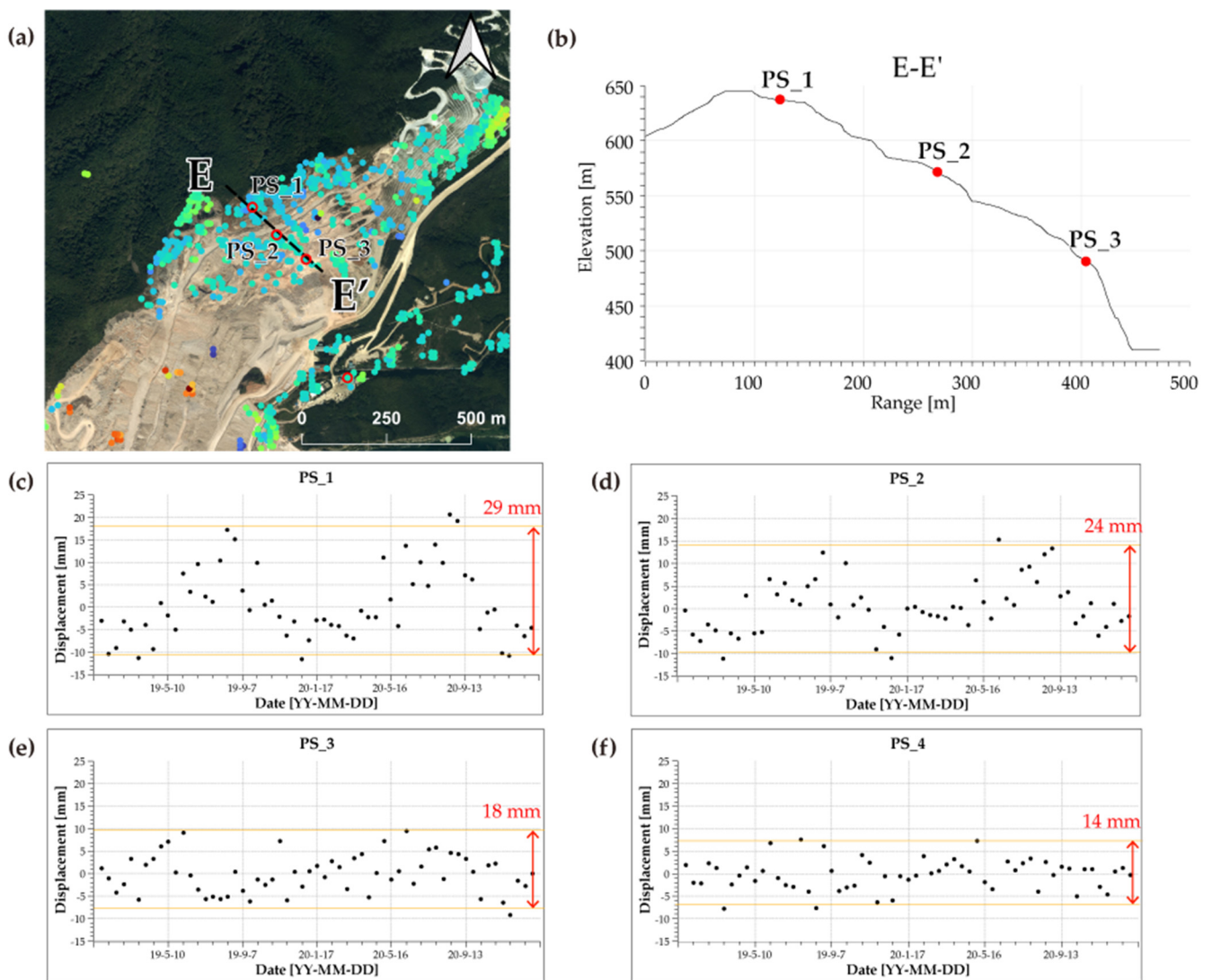
Figure 12. Seasonal LOS displacement trend in a time-series plot of PS_1, PS_2, and PS_3 from the PSInSAR images. (**a**) PSInSAR result in limestone rock, (**b**) a profile of E-E' with Copernicus DEM, time-series plots of displacement in the (**c**) PS_1, (**d**) PS_2, (**e**) PS_3, and (**f**) PS_4. PS_4 is selected at the lower point in a valley for comparison.

We attempted a very rough calculation of the thermal expansion of the limestone rocks, assuming a volume expansion of a point target occurring equally in every direction. The thermal expansion of a material, ΔL, can be calculated by

$$\Delta L = L \times \alpha \times \Delta T, \tag{7}$$

where L is the length of the material, α is the thermal expansion coefficient measured in [/°C], and ΔT is the change in temperature. In Figure 12c–f, the widths of the seasonal displacement variation (ΔL) of PS_1, PS_2, and PS_3 were about 29 mm, 24 mm, and 18 mm, respectively. PS_4 was selected on the stable roof of the building at the bottom of the valley and showed no seasonal variation, with a width of 14 mm, which is close to the overall noise level of PSInSAR. The higher the elevation is, the larger the variation is for PS_1, PS_2, and PS_3. Assuming that the rock is fixed at the bottom of the exposed rock with no soil or vegetation cover, we can relate the height of each PS to the length (*L*) of the rock exposed to air along the slope, as shown in Table 4. We also assume that the thermal expansion on each PS is isotropic, i.e., having identical values in all directions, so that LOS directional measurement can be used directly in the calculation of Equation (7). The seasonal temperature change (ΔT) is roughly 40 °C, with the lowest being −10 °C and the

highest being 30 °C in the study area. The thermal expansion coefficients of PS_1, PS2, and PS_3 were calculated to be about $1.9 \times 10^{-6}/°C$, $2.5 \times 10^{-6}/°C$, and $5.0 \times 10^{-6}/°C$, respectively. The average of those values is $3.1 \times 10^{-6}/°C$, which is slightly less than, but at least in accordance with the same order of pure limestone ($4\sim8 \times 10^{-6}/°C$) [46]. Considering that the open-pit mine is composed of low-grade limestone, the calculated values are somewhat within a reasonable range.

Figure 13 shows a time-series plot of the transmission tower for electricity, which has larger seasonal variations in displacement than the limestone outcrops. The thermal expansion coefficient of the tower was calculated to be $9.3 \times 10^{-6}/°C$, as shown in Table 3. It is three times larger than the limestone outcrops and is similar to that of pure iron ($11 \times 10^{-6}/°C$). There are many assumptions in the above calculations that need further study, especially in terms of the isotropic direction of the thermal expansion and the effective length of body under a thermal condition. However, it is encouraging that the values calculated in this new method are within a reasonable range when compared with the inventory of materials.
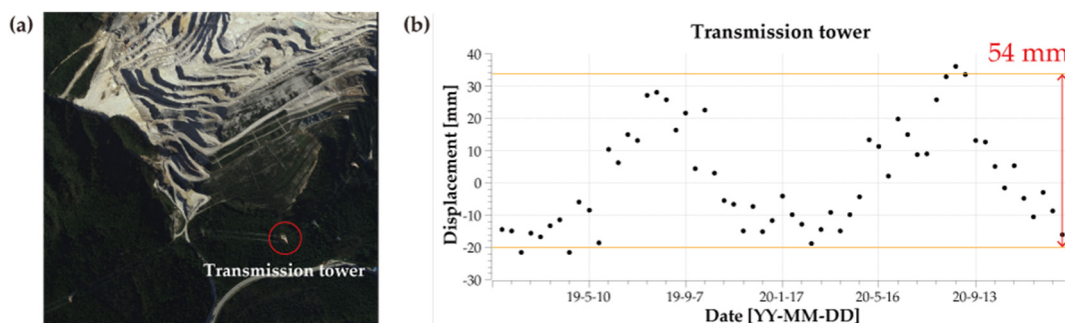
Figure 13. Seasonal LOS displacement of a transmission tower located near the mining area, as shown in the left aerial photograph taken in 2021. (**a**) Transmission tower; (**b**) time-series plots of displacement in transmission tower.

Table 4. Calculation of the thermal expansion coefficients of exposed limestone rocks and the transmission iron tower.

Type	Limestone PS1	Limestone PS2	Limestone PS3	Transmission Tower
Length (L) [m]	394	242	90	145
LOS displacement (ΔL) [mm]	29	24	18	54
Thermal Expansion Coefficient (α) [$10^{-6}/°C$]	1.9	2.5	5.0	9.3
α of Pure Material [$10^{-6}/°C$]	4~8 (Limestone)			11 (Iron)

5. Discussion

We used InSAR-generated DEMs to roughly calculate the elevation changes and divide the relevant regions into the mining, storage, and mined-out areas. Care must be taken when using these DEMs because SRTM DEM was obtained in the wintertime (February 2000), while Copernicus DEM was averaged over a period between August 2011 and August 2014. Seasonal variations on the vegetation canopy might have caused less penetration and, thus, a higher elevation in the X-band of Copernicus DEM in the summertime than the C-band of SRTM DEM in wintertime. Therefore, a direct comparison between the two DEMs should be valid in a bald area with no vegetation cover. The various DEMs used in the cross-sections of Figures 7, 9 and 11 were obtained from the National Geographic Information Service [25], which has a better resolution of 1 m than that of the InSAR DEMs using a 30 m grid. They were produced by aerial stereo photogrammetry with limited coverage over the study area and may be inconsistent with the InSAR-generated DEMs due to the geometric distortions of SAR.

The Copernicus DEM used for PSInSAR has a time difference of about 5 years (from the SAR dataset). Therefore, a DEM error map was estimated and subtracted from the LOS velocity map during the PSInSAR to correct the DEM error.

Coherence imagery is efficient for detecting random changes during the study period. However, only the descending data were used (Table 1) due to the missing data in the ascending orbit. When compared with 90 descending data, there were only 54 data points from the ascending orbit. The geometric distortions from the coherence images from the ascending and descending data are quite different from each other, especially for these highly sloping targets. Any attempt to geometrically merge the coherence from two different orbits has failed due to the foreshortening and layover effects, especially on the east- or west-facing slopes. Spatial decorrelation on radar-facing slopes should be identified and excluded from coherence imagery, which might be misinterpreted as temporal decorrelation otherwise [13].

Out of the total 35 parameters for StaMPS, we only adjusted the five most influential parameters, as shown in Table 2. We started the processing with the values used by Höser [32], who studied landslides. We then adjusted the parameter furthermore to find a more suitable value. For example, unwrapping errors are mostly caused by spatially correlated look-angle (SCLA) errors. We set scla_deramp to 'Y' so that the SCLA error is estimated from the unwrapped interferogram, and the error is reduced by subtracting it from the unwrap step. The unwrap_grid_size parameter can be increased when the unwrapping result is not smooth enough. However, setting a unwrap_grid_size value that is too large may damage the original value, so an appropriate parameter should be set using the user's discretion.

In order to synthesize the displacement components of the ascending and descending data obtained from the PSInSAR results, IDW interpolation was applied to the PS points, and the dataset was converted into raster data. Then, Equation (5) was applied to obtain the horizontal and vertical components of the displacement. However, the reliability of the interpolation is low in areas with sparse PS data density. Therefore, we only plotted the cross-sections along the area with high PS density for both the ascending and descending data. This was the reason why we needed to reduce the data duration for PSInSAR for two years (from 2019 to 2020), even though we have a dataset from 2018 to 2020. We wanted to increase the PS population, especially in the tailings storage area. The red and yellow colors in the RGB-composite of the yearly averaged coherence image in Figure 8b prevents the yielding of PS in those areas due to the low coherence in 2018. Therefore, coherence imagery can be useful in selecting the duration of input data for the PSInSAR technique.

The seasonal variations of the PSInSAR displacements on the limestone bedrock and iron transmission tower were interpreted as temporal expansions of the materials. However, there are still many other explanations (during the PSInSAR processing), such as the seasonal variation in atmospheric delay or uncorrected DEM errors, that need further study. The derivation of the temporal expansion coefficient using Equation (7) also needs to be improved further to incorporate the volumetric thermal expansion model rather than the simple linear expansion model. However, it is still encouraging to obtain the thermal expansion coefficients of the materials that are similar to those in the literature.

6. Conclusions

In this study, the activity in the Okgye open-pit limestone mine was analyzed by applying various techniques, such as InSAR DEM, InSAR coherence, and PSInSAR using a Sentinel-1 satellite dataset. Using SRTM 1Sec HGT DEM and Copernicus 30m DEM, elevation change data were produced to estimate a total of 39.13 million tons of clinker production from 2000 to 2014. A time-series analysis of 12-day coherence images and an RGB-composite of the annually averaged coherence images confirmed the random change in surface scatterers and the activity of the mines, especially where roads were built, or tailings dumping was carried out. Persistent scatterers were generated in stable points where

ground subsidence was observed using the PSInSAR technique. Continuous subsidence has occurred in the areas where tailings were dumped in the past and in the restored slopes. The LOS displacements from the ascending and descending orbits were converted into east and vertical components. The largest displacement of 18~45 mm/year occurred in the tailings storage area, where tailings were dumped until 2018. The restored slopes in the three different regions showed subsidence of 5~11 mm/year in the mining area, 6~16 mm/year in the tailings storage area, and 7~16 mm/year in the mined-out area, depending on the time after slope restoration was completed. For the time-series plot of each PS, the seasonal variation was interpreted as a thermal expansion to estimate the thermal expansion coefficient values that were similar to the theoretical values.

Through this study, it was confirmed that various SAR techniques could be effectively used in the analysis of activities in open-pit mines. A combination of time-series coherence imagery and PSInSAR techniques can provide not only the observation of stable targets but also random changes. It is expected that the InSAR methods presented in this study represent very strong monitoring tools for open-pit mines. In order to verify the results, a set of field measurements need to be redesigned to meet the accuracy and characteristics of the InSAR techniques.

Author Contributions: Conceptualization, H.L. (Hoseung Lee), J.M., and H.L. (Hoonyol Lee); methodology, H.L. (Hoseung Lee), J.M., and H.L. (Hoonyol Lee); software, H.L. (Hoseung Lee); validation, H.L. (Hoseung Lee), J.M., and H.L. (Hoonyol Lee); formal analysis, H.L. (Hoseung Lee) and H.L. (Hoonyol Lee); investigation, H.L. (Hoseung Lee), J.M., and H.L. (Hoonyol Lee); resources, H.L. (Hoonyol Lee); data curation, H.L. (Hoseung Lee); writing—original draft preparation, H.L. (Hoseung Lee); writing—review and editing, J.M., and H.L. (Hoonyol Lee); visualization, H.L. (Hoseung Lee); supervision, H.L. (Hoonyol Lee); project administration, H.L. (Hoonyol Lee); funding acquisition, H.L. (Hoonyol Lee) All authors have read and agreed to the published version of the manuscript.

Data Availability Statement: The data presented in this study are available on request from the corresponding author.

Conflicts of Interest: The authors declare no conflict of interest.

References

1. Hu, H.; Fernández-Steeger, T.M.; Dong, M.; Azzam, R. Deformation Monitoring and Modeling Based on LiDAR Data for Slope Stability Assessment. In Proceedings of the 19. Tagung Für Ingenieurgeologie, Munich, Germany, 13–16 March 2013.
2. Lee, S.; Jang, Y. Stability Assesment of the Slope at the Disposal Site of Waste Rock in Limestone Mine. *Tunn. Undergr. Space* **2010**, *20*, 475–490.
3. Carlà, T.; Intrieri, E.; Raspini, F.; Bardi, F.; Farina, P.; Ferretti, A.; Colombo, D.; Novali, F.; Casagli, N. Perspectives on the Prediction of Catastrophic Slope Failures from Satellite InSAR. *Sci. Rep.* **2019**, *9*, 1–9. https://doi.org/10.5194/egusphere-egu2020-13158.
4. Blikra, L.H.; Fasani, G.B.; Esposito, C.; Lenti, L.; Martino, S.; Pecci, M.; Mugnozza, G.S.; Kalenchuk, K.S.; Hutchinson, D.J.; Diederichs, M. 26 the Aknes Rockslide, Norway. In *Landslides: Types, Mechanisms and Modeling*; Cambridge University Press: Cambridge, UK, 2012; p. 323.
5. Michoud, C.; Bazin, S.; Blikra, L.H.; Derron, M.; Jaboyedoff, M. Experiences from Site-Specific Landslide Early Warning Systems. *Nat. Hazards Earth Syst. Sci.* **2013**, *13*, 2659–2673. https://doi.org/10.5194/nhess-13-2659-2013.
6. United Nations system for disaster risk reduction (UNISDR), U. UNISDR Terminology on Disaster Risk Reduction: United Nations Office on Disaster Risk Reduction, Geneva, 2009.
7. Ferretti, A.; Monti-Guarnieri, A.V.; Prati, C.M.; Rocca, F.; Massonnet, D. *InSAR Principles: Guideline for SAR Interferometry Processing and Interpretation*; ESA Publication: Noordwijk, The Netherlands, 2007.
8. Carlà, T.; Farina, P.; Intrieri, E.; Ketizmen, H.; Casagli, N. Integration of Ground-Based Radar and Satellite InSAR Data for the Analysis of an Unexpected Slope Failure in an Open-Pit Mine. *Eng. Geol.* **2018**, *235*, 39–52. https://doi.org/10.1016/j.enggeo.2018.01.021.

9. Casagli, N.; Catani, F.; Del Ventisette, C.; Luzi, G. Monitoring, Prediction, and Early Warning using Ground-Based Radar Interferometry. *Landslides* **2010**, *7*, 291–301. https://doi.org/10.1007/s10346-010-0215-y.

10. Casagli, N.; Frodella, W.; Morelli, S.; Tofani, V.; Ciampalini, A.; Intrieri, E.; Raspini, F.; Rossi, G.; Tanteri, L.; Lu, P. Spaceborne, UAV and Ground-Based Remote Sensing Techniques for Landslide Mapping, Monitoring and Early Warning. *Geoenvironmental Disasters* **2017**, *4*, 1–23. https://doi.org/10.1186/s40677-017-0073-1.

11. Hanssen, R.F. *Radar Interferometry: Data Interpretation and Error Analysis*; Springer Science & Business Media: Berlin, Germany, 2001. https://doi.org/10.1007/0-306-47633-9.

12. Ferretti, A.; Prati, C.; Rocca, F. Permanent Scatterers in SAR Interferometry. *IEEE Trans. Geosci. Remote Sens.* **2001**, *39*, 8–20. https://doi.org/10.1109/36.898661.

13. Lee, H.; Liu, J.G. Analysis of Topographic Decorrelation in SAR Interferometry using Ratio Coherence Imagery. *IEEE Trans. Geosci. Remote Sens.* **2001**, *39*, 223–232. https://doi.org/10.1109/36.905230.

14. Han, H.; Kim, Y.; Jin, H.; Lee, H. Analysis of Annual Variability of Landfast Sea Ice Near Jangbogo Antarctic Station using InSAR Coherence Images. *Korean J. Remote Sens.* **2015**, *31*, 501–512. https://doi.org/10.7780/kjrs.2015.31.6.1.

15. Moon, J.; Lee, H. Analysis of Activity in an Open-Pit Mine by using InSAR Coherence-Based Normalized Difference Activity Index. *Remote Sens.* **2021**, *13*, 1861. https://doi.org/10.3390/rs13091861.

16. Paradella, W.R.; Ferretti, A.; Mura, J.C.; Colombo, D.; Gama, F.F.; Tamburini, A.; Santos, A.R.; Novali, F.; Galo, M.; Camargo, P.O. Mapping Surface Deformation in Open Pit Iron Mines of Carajás Province (Amazon Region) using an Integrated SAR Analysis. *Eng. Geol.* **2015**, *193*, 61–78. https://doi.org/10.1016/j.enggeo.2015.04.015.

17. Hartwig, M.E.; Paradella, W.R.; Mura, J.C. Detection and Monitoring of Surface Motions in Active Open Pit Iron Mine in the Amazon Region, using Persistent Scatterer Interferometry with TerraSAR-X Satellite Data. *Remote Sens.* **2013**, *5*, 4719–4734. https://doi.org/10.3390/rs5094719.

18. Hallacement. Available online: https://www.hallacement.co.kr/company/siteguide (accessed on 1 August 2022).

19. Kim, M.; Kim, K. *Seokbyeongsan Area (Limestone) Detailed Geological Survey Report*; Korea Mine Rehabilitation and Mineral Resources Corporation: Wonju-si, Republic of Korea, 2020.

20. Lee, H.J.; Kim, S.Y.; Jang, B.J.; Kim, K.D. Analysis and Selection of Ganwon-do Open-Pit Mine Monitoring Target Area. In Proceedings of the 2014 Conference on the Geospatial Information, Incheon, Korea, November 2014; pp. 91–92.

21. Kim, K.; Joo, P.; Kim, H. A Study of Rehabilitation for Limestone Quarry Near Baekdu Daegan Mountain System (1)-in Case Study for Hydroseeding Experiment on Okke Quarry. *J. Korean Soc. Environ. Restor. Technol.* **2011**, *14*, 55–66. https://doi.org/10.13087/kosert.2011.14.4.055.

22. Kim, K.; Kim, H. A Study of Rehabilitation for Limestone Quarry Near the Baekdudaegan Mountains (2)-in Case Study for Planting Seedlings Experiment on Okke Quarry. *J. Korean Soc. Environ. Restor. Technol.* **2012**, *15*, 117–125. https://doi.org/10.13087/kosert.2012.5.2.117.

23. Earthexplorer. Available online: https://earthexplorer.usgs.gov (accessed on 26 January 2022).

24. CREODIAS Finder. Available online: https://finder.creodias.eu (accessed on 26 January 2022).

25. National Geographic Information Service. Available online: https://map.ngii.go.kr/ms/map/NlipMap.do (accessed on 21 August 2022).

26. Copernicus Open Access Hub. Available online: https://scihub.copernicus.eu/dhus/#/home (accessed on 26 January 2022).

27. ASF Data Search Vertex. Available online: https://search.asf.alaska.edu/#/?dataset=AVNIR (accessed on 21 September 2022).

28. Jaber, W.A.; Floricioiu, D.; Rott, H.; Eineder, M. Surface Elevation Changes of Glaciers Derived from SRTM and TanDEM-X DEM Differences. In Proceedings of the 2013 IEEE International Geoscience and Remote Sensing Symposium-IGARSS, Melbourne, VIC, Australia, 21–26 July 2013; pp. 1893–1896. https://doi.org/10.1109/igarss.2013.6723173.

29. Parwata, I.N.S.; Nakashima, S.; Shimizu, N.; Osawa, T. Effect of Digital Elevation Models on Monitoring Slope Displacements in Open-Pit Mine by Differential Interferometry Synthetic Aperture Radar. *J. Rock Mech. Geotech. Eng.* **2020**, *12*, 1001–1013. https://doi.org/10.1016/j.jrmge.2020.01.003.

30. Hooper, A.; Segall, P.; Zebker, H. Persistent Scatterer Interferometric Synthetic Aperture Radar for Crustal Deformation Analysis, with Application to Volcán Alcedo, Galápagos. *J. Geophys. Res. Solid Earth* **2007**, *112*. https://doi.org/10.1029/2006jb004763.

31. Wang, Q.; Yu, W.; Xu, B.; Wei, G. Assessing the use of GACOS Products for SBAS-INSAR Deformation Monitoring: A Case in Southern California. *Sensors* **2019**, *19*, 3894. https://doi.org/10.3390/s19183894.

32. Höser, T. Analysing the capabilities and limitations of InSAR using Sentinel-1 data for landslide detection and monitoring. Master's Thesis, University of Bonn, Bonn, Germany, 2018.

33. Cian, F.; Blasco, J.M.D.; Carrera, L. Sentinel-1 for Monitoring Land Subsidence of Coastal Cities in Africa using PSInSAR: A Methodology Based on the Integration of SNAP and StaMPS. *Geosciences* **2019**, *9*, 124. https://doi.org/10.3390/geosciences9030124.

34. Delgado Blasco, J.M.; Foumelis, M.; Stewart, C.; Hooper, A. Measuring Urban Subsidence in the Rome Metropolitan Area (Italy) with Sentinel-1 SNAP-StaMPS Persistent Scatterer Interferometry. *Remote Sens.* **2019**, *11*, 129. https://doi.org/10.3390/rs11020129.

35. Li, Z.; Muller, J.; Cross, P.; Fielding, E.J. Interferometric Synthetic Aperture Radar (InSAR) Atmospheric Correction: GPS, Moderate Resolution Imaging Spectroradiometer (MODIS), and InSAR Integration. *J. Geophys. Res. Solid Earth* **2005**, *110*. https://doi.org/10.1029/2004jb003446.

36. Bekaert, D.; Walters, R.J.; Wright, T.J.; Hooper, A.J.; Parker, D.J. Statistical Comparison of InSAR Tropospheric Correction Techniques. *Remote Sens. Environ.* **2015**, *170*, 40–47. https://doi.org/10.1016/j.rse.2015.08.035.

37. Bekaert, D.; Hooper, A.; Wright, T.J. A Spatially Variable Power Law Tropospheric Correction Technique for InSAR Data. *J. Geophys. Res. Solid Earth* **2015**, *120*, 1345–1356. https://doi.org/10.1002/2014jb011558.

38. Yu, C.; Penna, N.T.; Li, Z. Generation of Real-time Mode High-resolution Water Vapor Fields from GPS Observations. *J. Geophys. Res. Atmos.* **2017**, *122*, 2008–2025. https://doi.org/10.1002/2016jd025753.

39. GIS-Blog. Available online: https://gitlab.com/Rexthor/gis-blog/-/blob/master/StaMPS/2-4_StaMPS-steps.md (accessed on 21 September 2022).

40. Tang, W.; Motagh, M.; Zhan, W. Monitoring Active Open-Pit Mine Stability in the Rhenish Coalfields of Germany using a Coherence-Based SBAS Method. *Int. J. Appl. Earth Obs. Geoinf.* **2020**, *93*, 102217. https://doi.org/10.1016/j.jag.2020.102217.

41. Jin, L.; Funning, G.J. Testing the Inference of Creep on the Northern Rodgers Creek Fault, California, using Ascending and Descending Persistent Scatterer InSAR Data. *J. Geophys. Res.: Solid Earth* **2017**, *122*, 2373–2389. https://doi.org/10.1002/2016jb013535.

42. Fuhrmann, T.; Garthwaite, M.C. Resolving Three-Dimensional Surface Motion with InSAR: Constraints from Multi-Geometry Data Fusion. *Remote Sens.* **2019**, *11*, 241. https://doi.org/10.3390/rs11030241.

43. Crosetto, M.; Monserrat, O.; Cuevas-González, M.; Devanthéry, N.; Luzi, G.; Crippa, B. Measuring Thermal Expansion using X-Band Persistent Scatterer Interferometry. *ISPRS J. Photogramm. Remote Sens.* **2015**, *100*, 84–91. https://doi.org/10.1016/j.isprsjprs.2014.05.006.

44. Lazecky, M.; Perissin, D.; Bakon, M.; de Sousa, J.M.; Hlavacova, I.; Real, N. Potential of Satellite InSAR Techniques for Monitoring of Bridge Deformations. In Proceedings of the 2015 Joint Urban Remote Sensing Event (JURSE), Lausanne, Switzerland, 30 March–1 April 2015; pp. 1–4. https://doi.org/10.1109/jurse.2015.7120506.

45. Cohen-Waeber, J.F. *Spatiotemporal Patterns of Seasonality in Landslide Deformation from InSAR and GPS.*; University of California, Berkeley, CA, USA, 2018.

46. Kim, K. Use of Low-Grade Limestone for Cement Industry as Concrete Aggregate. *Mag. RCR* **2016**, *11*, 20–23. https://doi.org/10.14190/MRCR.2016.11.1.020.